

Visualization of Heterogeneous Oxygen Storage Behavior in Three-Way Catalyst Pt/Ce₂Zr₂O_x Particles by Hard X-ray Spectro-ptychography

Makoto Hirose,^[a,b] Nozomu Ishiguro,^[b] Kei Shimomura,^[a,b] Nicolas Burdet,^[b] Hirosuke Matsui,^[c] Mizuki Tada,^{*[b,c]} and Yukio Takahashi^{*[a,b]}

Abstract: The cerium density and valence in micrometer-size Pt/Ce₂Zr₂O_x (x=7–8) three-way catalyst particles were successfully mapped by hard X-ray spectro-ptychography (ptychographic-XAFS). The analysis of correlation between the Ce density and valence in ptychographic-XAFS images suggested the existence of several oxidation behaviors in the oxygen storage process in the Ce₂Zr₂O_x particles. Ptychographic-XAFS will open up the nanoscale chemical imaging and structural analysis of heterogeneous catalysts.

Heterogeneous solid catalysts are key materials in various chemical processes in modern industry, and the intrinsic complexity of their heterogeneous structures has led to various discussions on their structure-activity relationship. The most typical form of solid catalysts is powder, which is an assembly of non-uniform particles with different sizes, morphologies, atomic components, surface structures, and mesoscopic domains. The complexity of their structural parameters is considered to be the reason for their unique catalytic performances; however, it is highly difficult to evaluate these heterogeneous structures in real space. Conventional characterization of average for a powder assembly obscures active parts in a heterogeneous solid catalyst.

Ce-based mixed oxides such as CeZrO_x are efficient oxygen storage/release materials and are widely used as a co-catalyst in three-way automobile exhaust systems to expand the narrow operation window. In particular, Ce₂Zr₂O_x (7 ≤ x ≤ 8) solid-solution oxide with an ordered arrangement of Ce and Zr has been reported to exhibit stoichiometric oxygen storage/release capacities (OSC), where approximately 90% of the bulk Ce atoms are used in the redox process between κ-phase Ce₂Zr₂O₈ and pyrochlore Ce₂Zr₂O₇,^[1] and the synthesis of pure Ce₂Zr₂O_x has been recently proposed.^[2] The origin of the high OSC of Ce₂Zr₂O_x has been widely investigated and is considered to be due to the small vacancy formation energy by local relaxation between ZrO₈ coordination and ZrO₆[V]₂ (V: vacancy), on the basis of

crystallographical studies,^[3] theoretical calculations,^[4] and time-resolved XAFS analysis.^[5] However, the heterogeneity of the mixed-oxide particles has prevented understanding of the real reaction behavior of OSC in the material.

X-ray imaging techniques, such as transmission and scanning X-ray microscopy using highly focused beams, are particularly promising tools in the field of microspectroscopy,^[6] in which the use of X-rays as a probe makes it possible to image both structures and chemical states through the absorption edges of a target element with a resolution of 30–100 nm. Also, an X-ray probe induces less radiation damage than a transmission electron microscope with an electron energy loss spectroscopy.^[7] The minimum probe size of the X-rays in practical use is ~30 nm in the soft X-ray region and ~100 nm in the hard X-ray region, which is limited by the difficulty of fabricating optical devices. So far, scanning spatially resolved X-ray absorption fine structure (XAFS) using Kirkpatrick–Baez (KB) focusing mirrors was applied to Ce₂Zr₂O_x particles, whose average size was 750 nm, and the heterogeneity of the Ce oxidation state and oxygen diffusion inside an individual particle was visualized for the first time.^[8] However, the focused beam size (a few hundred nm) was limited in principle, and a practical imaging technique with much higher spatial resolution is required for the further exploration of their structural correlation.

X-ray ptychography^[9] can in principle overcome the limitations of X-ray optics, in which a sample is scanned across a coherent X-ray probe, the coherent diffraction pattern is observed at each beam position, and then images of both the sample and probe are reconstructed using iterative phase retrieval calculation. X-ray ptychography using multiple energies including the absorption edge of a specific element, which is often referred to as X-ray spectro-ptychography, has been demonstrated in the soft X-ray region, which has been applied to the study of delithiation in LiFePO₄ nanoplates^[10] to understanding Fe

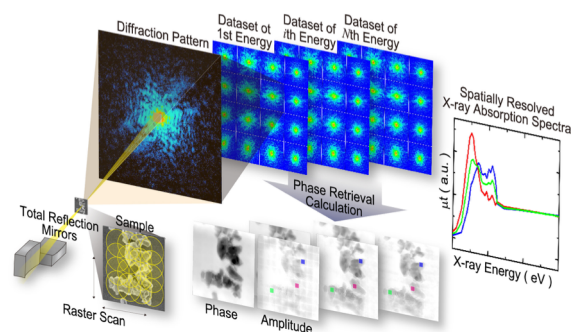


Figure 1. Schematic of X-ray spectro-ptychography (ptychographic-XAFS). A focused coherent X-ray beam is scanned across the specimen at multiple X-ray energies. Phase and amplitude images are reconstructed from diffraction patterns by phase retrieval calculation. By analyzing the energy dependence of the reconstructed images, spatially resolved X-ray absorption spectra are derived.

[a] M. Hirose, K. Shimomura, Prof. Dr. Y. Takahashi
Department of Engineering, Graduate School of Osaka University
Yamada-oka, Suita, Osaka, 565-0871, Japan
E-mail: takahashi@prec.eng.osaka-u.ac.jp

[b] M. Hirose, Dr. N. Ishiguro, K. Shimomura, Dr. N. Burdet,^[1] Prof. Dr. M. Tada, Prof. Dr. Y. Takahashi
RIKEN SPring-8 Center
Kouto, Sayo-cho, Sayo, Hyogo, 679-5148, Japan.
[†] Current address: Advanced Light Source, Lawrence Berkeley National Laboratory, Berkeley, CA 94720

[c] Dr. H. Matsui, Prof. Dr. M. Tada
Department of Chemistry, Research Center for Materials Science/Graduate School of Science, Nagoya University
Furo-cho, Chikusa, Nagoya, Aichi, 464-8602, Japan
E-mail: mtada@chem.nagoya-u.ac.jp
Supporting information for this article is given via a link at the end of the document.

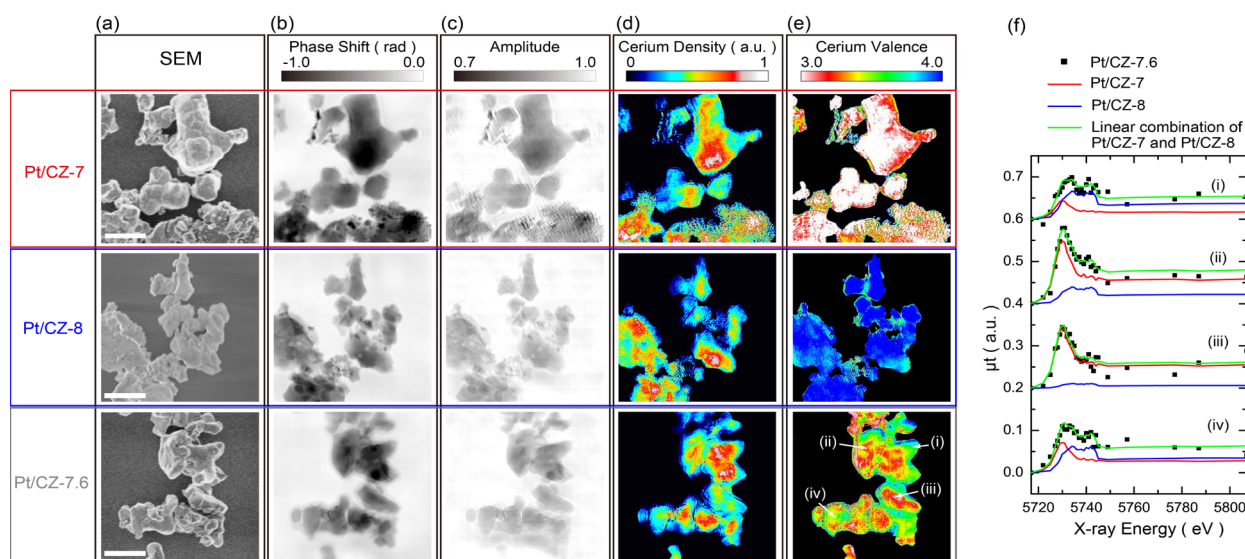


Figure 2. (a–e) Images of the Pt/CZ-7, Pt/CZ-8, and Pt/CZ-7.6 particles. The scale bar is 1 μm . (a) FE-SEM images. (b and c) Phase and amplitude images at 5.732 keV (d) Ce density maps. (e) Ce valence maps. The pixel size of the images in (b–e) is 13 nm. (f) One-pixel XANES spectra at particular positions (i)–(iv) marked in (e) of Pt/CZ-7.6. Red, blue, and green lines present the fitted spectra of Pt/CZ-7, Pt/CZ-8, and their linear combination, respectively.

deposition in fluid catalytic cracking catalysis.^[11] Extending this approach to the hard X-ray region enables us to visualize the chemical state of nanostructures buried within thick samples. However, the absorption of incident X-rays is weak in the hard X-ray region, which results in the deterioration of convergence in the phase retrieval calculation. Recently, a phase retrieval algorithm with a constraint based on the Kramers–Kronig relation (KKR) has been proposed and more quantitative images as well as X-ray absorption spectra have been experimentally obtained.^[12]

In this paper, we demonstrate the visualization of Ce density and valence distribution of micron-sized Pt/Ce₂Zr₂O_x (7 ≤ x ≤ 8) particles at better than 50 nm resolution by hard X-ray spectro-ptychography (ptychographic-XAFS) with phase retrieval using the KKR constraint (Fig. 1). The statistical analysis of correlation between the cerium density and valence in the ptychographic-XAFS images suggested the existence of several oxidation behaviors in the oxygen storage process in the material.

1 wt% Pt-supported Ce₂Zr₂O_x particles (average Ce₂Zr₂O_x particle size = 750 nm)^[1,8a] were treated with H₂ or O₂ to prepare (1) Pt/Ce₂Zr₂O₇ (denoted as Pt/CZ-7), fully reduced by H₂ at 873 K; (2) Pt/Ce₂Zr₂O₈ (denoted as Pt/CZ-8), fully oxidized by O₂ at 773 K; (3) Pt/Ce₂Zr₂O_{7.6} (denoted as Pt/CZ-7.6), prepared by the reaction of Pt/CZ-7 with O₂ at 423 K (details in SI 1). Average oxygen composition in Pt/CZ-7.6 were estimated by the analysis of the (440) peak positions of their XRD patterns (Fig. S1). The prepared particles were dispersed on 500-nm-thick Si₃N₄ membranes, and the hard X-ray ptychographic-XAFS measurements were performed using X-rays (5.717–5.817 keV, including the Ce L₃ edge) at the BL29XUL beamline, SPring-8 (Fig. S2 and details in SI 2). The amplitude and phase images were reconstructed using the ePIE algorithm^[13] with the KKR constraint^[12] (details in SI 3).

Figure 2(a) shows field-emission scanning electron microscopy (FE-SEM) images of the Pt/CZ particles. Figures 2(b) and (c) show phase and amplitude images at 5.732 keV above the Ce L₃ edge, respectively, of the Pt/CZ particles. Making use of the small-angle-geometry approximation, the real-space pixel

size of the reconstructed images is 13 nm. Based on the phase retrieval transfer function, the full-period spatial resolution was estimated to be better than 50 nm (Fig. S3). The spatial resolution obtained here is one order of magnitude higher than that of previous results.^[6] The shapes of the individual particles are in good agreement with the FE-SEM and X-ray ptychography images. XAFS spectrum can be derived using the relation $\mu t = -2\ln|T|$, where μ is the mass absorption coefficient, t is the local sample thickness, and $|T|$ is the amplitude image. X-ray absorption near-edge structure (XANES) spectra of Pt/CZ-7 and Pt/CZ-8 particles were averaged over all the particles present in the field of view and then normalized at the isosbestic point of 5.7697 keV (Fig. S4). Ce L₃-edge XANES is sensitive to valence and the obtained XANES spectra of Pt/CZ-7 and Pt/CZ-8 are in good agreement with those in previous reports (Fig. 2(f)).^[8bc]

The Ce density and valence maps of the Pt/CZ-7.6 particles were then estimated by the analysis of the ptychographic-XAFS images. The XANES spectra of Pt/CZ-7.6 can be approximately expressed by a linear combination of the normalized XANES spectra of Pt/CZ-7 and Pt/CZ-8 as

$$(\mu t)_{\text{CZ7.6}} = a(\mu t)_{\text{CZ7}} + b(\mu t)_{\text{CZ8}} \quad [\text{Eq. (1)}],$$

where a and b are coefficients. The parameters a and b at each pixel were determined by a least-squares fit (details in SI 4). $a+b$ and $(3a+4b)/(a+b)$ correspond to the Ce density and valence, respectively (Figs. 2(d) and (e)).

We investigated correlation between the Ce density and valence in the two-dimensional images (Figs. 2(d) and (e)) to visualize differences in the oxygen storage behaviors in local domains in the heterogeneous Ce₂Zr₂O_x particles (details in SI 5). The two-dimensional images of Pt/CZ-7.6 were divided into domains with particular sizes, e.g., 65 × 65 nm² (5 × 5 pixels) and 130 × 130 nm² (10 × 10 pixels), and the Ce density and valence in a domain were independently plotted (Figs. 3(b), S7, and S8). For example, a domain with 5 × 5 binning has the 25 data sets of the Ce density and valence. If the density-valence plot of the 25 data sets shows a particular correlation, a reaction behavior in the domain of 65 × 65 nm² can be discussed. Judging from the facts

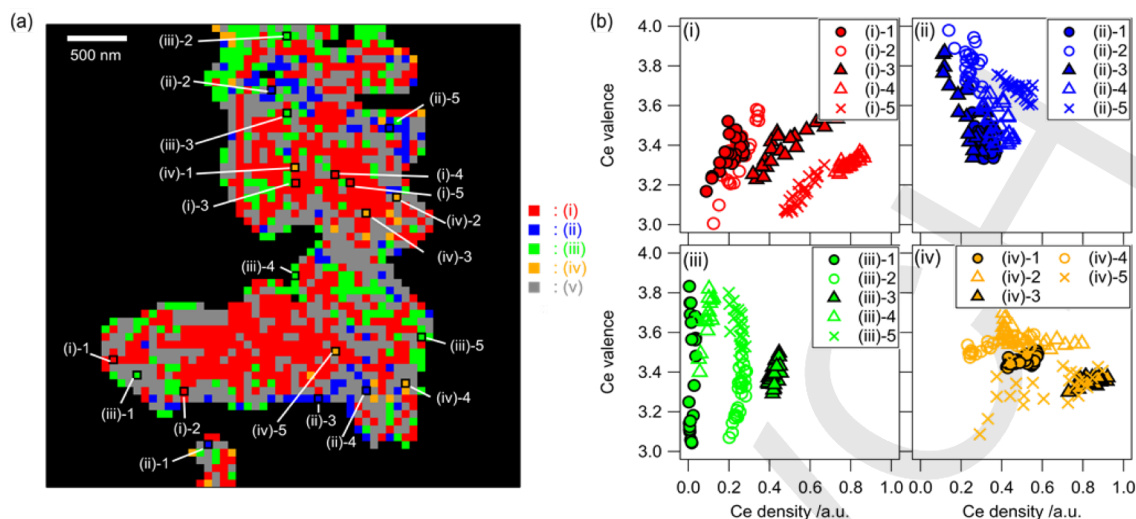


Figure 3. (a) Distribution of domains ($65 \times 65 \text{ nm}^2$) assigned to five groups by the statistical correlation analysis of the Ce density and Ce valence of Pt/CZ-7.6. (i) Positive correlation (red), (ii) negative correlation (blue), (iii) quasi-constant Ce density (green), (iv) quasi-constant Ce valence (yellow), and (v) no correlation (gray). (b) Ce density-Ce valence plots of the domains belonging to the correlation groups (i)-(iv). The positions of the domains in (b) are marked in (a).

that 10×10 binning provided a blurred image with a large ratio of no-correlation domains (20.8%) (Fig. S8) and 5×5 binning was similar to the actual spatial resolution of the spectro-ptychography (Fig. S3), we decided to use 5×5 binning for further analysis.

Note that there are several types of the correlations in the density-valence plots, which are classified into five groups by the different trends: (i) positive correlation; (ii) negative correlation; (iii) quasi-constant Ce density; (iv) quasi-constant Ce valence; and (v) no correlation as shown in Fig. 3. Considering the fact that the Ce density reflects the thickness of the sample in the two-dimensional projection image, a part with a large Ce density contains the information of bulk and that with a small Ce density shows that of surface. Group (i) presented in red in Fig. 3(a) shows a positive gradient in the density-valence plot Fig. 3(b-i), suggesting that the bulk of $\text{Ce}_2\text{Zr}_2\text{O}_x$ was oxidized rather than the surface. The red domains assigned to group (i) accounted for 41% of the particles in Fig. 3(a) and was mainly found at the core of the particles. In addition, most of the domains assigned to group (i) were observed to have low Ce valence states of between 3 and 3.5 as shown in Fig. 3(b-i).

On the other hand, the majority of group (ii) with negative correlation was distributed in the subsurface region of the particles presented in blue in Fig. 3(a). The fraction of group (ii) was 7%. It was found that the Ce valence state of the domains assigned to group (ii) tended to be higher than 3.5, showing a different trend from group (i) (Fig. 3(b-ii)).

Group (iii) with a quasi-constant Ce density spread between Ce^{3+} and Ce^{4+} was distributed at particular parts with low Ce density (green domains in Figs. 3(a) and (b-iii)), for example, bridging parts between particles. The wide range of the Ce valence of group (iii) suggests the heterogeneity of the oxidation behavior in the domains, showing the complexity of interface structures of the particles. Group (iv) presented in yellow accounted for a small area and showed a quasi-constant Ce valence state between $\text{Ce}^{3.4+}$ and $\text{Ce}^{3.6+}$, indicating the existence of a metastable phase of $\text{Ce}^{3.5+}$. The ratio of domains with high error range of Ce valence (> 0.5) was only 1.7% of all domains by 5×5 binning and they were located at regions with low Ce density.

As the Pt/CZ-7.6 sample was prepared by the partial oxidation of reduced Pt/CZ-7 with O_2 at 423 K, it is reasonable that the Ce valence was higher at the particle surface exposed to O_2 , accounting for the negative gradient of group (ii). In contrast, if oxygen diffusion in $\text{Ce}_2\text{Zr}_2\text{O}_x$ bulk is faster than O_2 dissociation at surface, the correlation between the Ce density and valence should be assigned to group (i) with the positive gradient. A report of the low activation energies (E_a) of Zr-O bond formation (4 kJ mol^{-1}) estimated by time-resolved XAFS suggests smooth oxygen diffusion in $\text{Ce}_2\text{Zr}_2\text{O}_x$ bulk for oxygen storage process.^[5]

Temperature-programmed oxidation (TPO) and thermogram (TG/DTG) analysis of Pt/CZ-7 showed two peaks at approximately 422 and 582 K^[3bc], suggesting the existence of the metastable phase of $\text{Ce}_2\text{Zr}_2\text{O}_{7.5}$, which was also confirmed by XRD analysis.^[3ab] The first oxidation peak at around 420 K corresponds to the oxidation of $\text{Ce}_2\text{Zr}_2\text{O}_7 \rightarrow \text{Ce}_2\text{Zr}_2\text{O}_{7.5}$ and the further oxidation ($\text{Ce}_2\text{Zr}_2\text{O}_{7.5} \rightarrow \text{Ce}_2\text{Zr}_2\text{O}_8$) proceeds at around 580 K. Thus, two different reaction behaviors crossing the metastable phase of $\text{Ce}_2\text{Zr}_2\text{O}_{7.5}$ can be observed at the oxidation temperature (423 K) of Pt/CZ-7.6, which is between the above temperatures.

In the first oxidation from $\text{Ce}_2\text{Zr}_2\text{O}_7$ to $\text{Ce}_2\text{Zr}_2\text{O}_{7.5}$, smooth oxygen diffusion in the phase with $x < 7.5$ proceeding at 420 K provides the reaction trend of group (i), which was mainly observed in the core of the CZ particles. In contrast, at surface parts with a low Ce density, sufficient oxygen supply brings about oxidation beyond the phase of $\text{Ce}_2\text{Zr}_2\text{O}_{7.5}$. As a result, relative decrease in the oxygen diffusion rate provides the different reaction behaviors of group (ii). Oxygen diffusion has been reported to proceed along the three-dimensional network in the $\langle 100 \rangle$, $\langle 010 \rangle$, and $\langle 001 \rangle$ directions.^[14] Oxygen may readily diffuse when vacancy sites are reasonably abundant ($x \sim 7$), while it may cause a jam in the network if the oxygen vacancies are already filled ($x > 7.5$). The differences in the reaction behaviors of groups (i) and (ii) would be related to the oxygen diffusion in the bulk. Group (v) without significant correlations accounts for several parts of the CZ particles and the improvement of spatial dissolution would decrease the fraction of group (v).

In this study, we successfully reconstructed the amplitude and phase images of ptychographic-XAFS at 27 X-ray energies to obtain two-dimensional mappings of the Ce density and valence of Pt/Ce₂Zr₂O_x particles. The statistical analysis of the correlation between the Ce density and valence clearly showed the existence of four different reaction behaviors in the oxygen storage process of Ce₂Zr₂O_x. Although structural differences in each domain are not yet clear, the heterogeneity of the mixed-oxide particles such as the boundaries of crystals, the location of defects is considered to be the cause of the different behaviors of the oxygen storage process in the solid particles. Three-dimensional imaging by a combination of computed tomography and ptychographic-XAFS is promising to elucidate the detail intrinsic heterogeneous reaction behaviors of the material. The spatial resolution of X-ray ptychography is decided only by the angular extent of scattered photons, while that of full-field transmission X-ray microscopy (FF-TXM), which achieves much faster measurements in a similar X-ray regime, is limited by the fabrication accuracy of X-ray optical devices which reaches technical limit. If we can use high coherent flux by the two orders of magnitude in the next-generation synchrotron facilities, X-ray ptychography will be a more promising and powerful tool to provide wide field-of-view and high spatial resolution with shorter exposure time compared with lens-based microscopy such as FF-TXM.

Experimental Section

Data collection: Ptychographic-XAFS experiment was performed in SPring-8 BL29XUL. 27 X-ray energies between 5.717 and 5.817 keV were selected and the finest energy gaps were 1 eV between 5.727 and 5.744 keV. Incident X-rays were two-dimensionally focused to a 500 nm (full width at half maximum) spot size by a pair of KB mirrors. The samples were placed in the focal plane and mounted on a piezoelectric stage inside a high-vacuum chamber. The Pt/CZ-x samples on 500-nm-thick Si₃N₄ membranes (SI 1) were scanned in 81 overlapping field of view with a step width of 400 nm. Multiple diffraction patterns were collected using an in-vacuum pixel array detector (Dectris EIGER 1M). The exposure time at each position was 4.0 s.

Image reconstruction and correlation analysis: The image reconstruction was performed by the ePIE algorithm using the KKR constraint. Initial guesses of the object function were unity, and initial guesses of the probe function were calculated in consideration of our experimental parameters. Iteration was continued for up to 2000 cycles, and the KKR constraint was used every 100 cycles to improve the quality of the reconstruction (SI 3). The detail of the correlation analysis of the Ce density and valence is presented in SI 5.

Acknowledgements

This work was supported by KAKENHI (Grant Nos. 16K13725, 16H00889, and Kiban B 26288005) and JSPS Fellows (Grant Nos. 16J00329 and 17J01673), and the SENTAN Project of JST. We thank Prof. Dr. K. Yamauchi (Osaka Univ.), Prof. Dr. T. Ishikawa (RIKEN), and Prof. Dr. M. Takata (Tohoku Univ./RIKEN) for many stimulating discussions, as well as Dr. Y. Kohmura (RIKEN) for

help in the experimental setup and Dr. Y. Nagai (Toyota Central R&D Labs. Inc.) for sample preparation.

Keywords: Three-way catalyst · ceria-zirconia · oxygen storage · X-ray spectro-ptychography

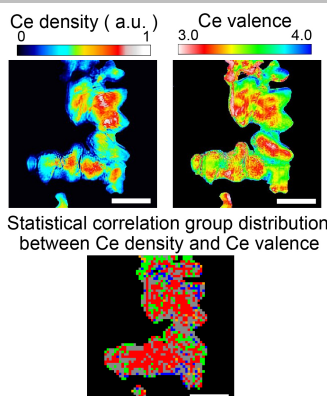
- [1] A. Suda, Y. Ukyo, H. Sobukawa, M. Sugiura, *J. Ceram. Soc. Jpn.*, **2002**, *110*, 126-130.
- [2] S. Urban, P. Dolcet, M. Möller, L. Chen, P. J. Klar, I. Djerdj, S. Gross, B. M. Smarsly, H. Over, *Appl. Catal. B Environ.*, **2016**, *197*, 23-34.
- [3] a) T. Sasaki, Y. Ukyo, K. Kuroda, S. Arai, S. Muto, H. Saka, *J. Ceram. Soc. Jpn.*, **2004**, *112*, 440-444; b) T. Sasaki, Y. Ukyo, A. Suda, M. Sugiura, K. Kuroda, S. Arai, H. Saka, *J. Ceram. Soc. Jpn.*, **2003**, *111*, 382-385; c) S. N. Achary, S. K. Sali, N. K. Kulkarni, P. S. R. Krishna, A. B. Shinde, A. K. Tyagi, *Chem. Mater.*, **2009**, *21*, 5848-5859.
- [4] a) H.-F. Wang, Y.-L. Guo, G.-Z. Lu, P. Hu, *Angew. Chem. Int. Ed.*, **2009**, *48*, 8289-8292; b) A. Gupta, A. Kumar, U. V. Waghmare, M. S. Hegde, *J. Phys. Chem. C*, **2017**, *121*, 1803-1808.
- [5] T. Yamamoto, A. Suzuki, Y. Nagai, T. Tanabe, F. Dong, Y. Inada, M. Nomura, M. Tada, Y. Iwasawa, *Angew. Chem. Int. Ed.*, **2007**, *46*, 9253-9256.
- [6] a) S. Bordiga, E. Groppo, G. Agostini, J. A. van Bokhoven, C. Lamberti, *Chem. Rev.*, **2013**, *113*, 1736-1850; b) Y. Suzuki, Y. Terada, Space-Resolved XAFS, Instrumentation and Applications, in *X-Ray Absorption and X-Ray Emission Spectroscopy: Theory and Applications*, Vol. I, (Eds. Jeroen A. van Bokhoven and Carlo Lamberti), John Wiley & Sons, Chichester (UK), **2016**, pp. 251-279; c) M. Tada, N. Ishiguro, Spatially Resolved XAFS, in *XAFS Techniques for Catalysts, Nanomaterials, and Surfaces*, (Eds: Y. Iwasawa, K. Asakura, and M. Tada), Springer, Switzerland, **2017**, pp. 133-147; d) K. H. Cats, B. M. Weckhuysen, *ChemCatChem*, **2016**, *8*, 1531-1542; e) I. L. C. Buurmans, B. M. Weckhuysen, *Nat. Chem.*, **2012**, *4*, 873-886; f) B. M. Weckhuysen, *Angew. Chem. Int. Ed.*, **2009**, *48*, 4910-4943; g) E. de Smit, I. Swart, J. F. Creemer, G. H. Hoveling, M. K. Gilles, T. Tyliczszak, P. J. Kooyman, H. W. Zandbergen, C. Morin, B. M. Weckhuysen, F. M. F. de Groot, *Nature*, **2008**, *456*, 222-225.
- [7] A. P. Hitchcock, J. J. Dynes, G. Johansson, J. Wang, G. Botton, *micron*, **2008**, *39*, 311-319.
- [8] a) M. Tada, N. Ishiguro, T. Uruga, H. Tanida, Y. Terada, S. Nagamatsu, Y. Iwasawa, S. Ohkoshi, *Phys. Chem. Chem. Phys.*, **2011**, *13*, 14910-14913; b) N. Ishiguro, T. Uruga, O. Sekizawa, T. Tsuji, M. Suzuki, N. Kawamura, M. Mizumaki, K. Nitta, T. Yokoyama, M. Tada, *ChemPhysChem*, **2014**, *15*, 1563-1568; c) H. Matsui, N. Ishiguro, K. Enomoto, O. Sekizawa, T. Uruga, M. Tada, *Angew. Chem. Int. Ed.*, **2016**, *55*, 12022-12025.
- [9] J. M. Rodenburg, A. C. Hurst, A. G. Cullis, B. R. Dobson, F. Pfeiffer, O. Bunk, C. David, K. Jefimovs, I. Johnson, *Phys. Rev. Lett.*, **2007**, *98*, 034801.
- [10] a) D. A. Shapiro, Y.-S. Yu, T. Tyliczszak, J. Cabana, R. Celestre, W. Chao, K. Kaznatcheev, A. L. D. Kilcoyne, F. Maia, S. Marchesini, Y. S. Meng, T. Warwick, L. L. Yang, H. A. Padmore, *Nat. Photonics*, **2014**, *8*, 765-769; b) Y.-S. Yu, C. Kim, D. A. Shapiro, M. Farmand, D. Qian, T. Tyliczszak, A. L. D. Kilcoyne, R. Celestre, S. Marchesini, J. Joseph, P. Denes, T. Warwick, F. C. Strobridge, C. P. Grey, H. Padmore, Y. S. Meng, R. Kosteci, J. Cabana, *Nano Lett.*, **2015**, *15*, 4282-4288; c) M. Farmand, R. Celestre, P. Denes, A. L. D. Kilcoyne, S. Marchesini, H. Padmore, T. Tyliczszak, T. Warwick, X. Shi, J. Lee, Y.-S. Yu, J. Cabana, J. Joseph, H. Krishnan, T. Perciano, F. R. N. C. Maia, D. A. Shapiro, *Appl. Phys. Lett.*, **2017**, *110*, 063101.
- [11] A. M. Wise, J. N. Weker, S. Kalirai, M. Farmand, D. A. Shapiro, F. Meirer, B. M. Weckhuysen, *ACS Catal.*, **2016**, *6*, 2178-2181.
- [12] M. Hirose, K. Shimomura, N. Burdet, Y. Takahashi, *Opt. Express*, **2017**, *25*, 8593-8603.
- [13] A. M. Maiden, J. M. Rodenburg, *Ultramicroscopy*, **2009**, *109*, 1256-1262.
- [14] M. Yashima, *Catal. Today*, **2015**, *253*, 3-19.

Entry for the Table of Contents

COMMUNICATION

Visualizing heterogeneous oxygen

storage behavior: Ce density and valence images of Pt/Ce₂Zr₂O_x particles were visualized with high spatial resolution by hard X-ray spectro-ptychography (ptychographic-XAFS). The statistical analysis of the correlation between Ce density and Ce valence showed the existence of four different reaction behaviors in the oxygen storage process. Scale bar: 1 μm.



Statistical correlation group distribution between Ce density and Ce valence

Makoto Hirose, Dr. Nozomu Ishiguro, Kei Shimomura, Dr. Nicolas Burdet, Dr. Hirosuke Matsui, Prof. Mizuki Tada, Prof. Dr. Yukio Takahashi**

Page No. – Page No.

Visualization of Heterogeneous Oxygen Storage Behavior in Three-Way Catalyst Pt/Ce₂Zr₂O_x Particles by Hard X-ray Spectro-Ptychography